

Investigating Nonlinear Quenching Effects on Polar Field Buildup in the Sun Using Physics-Informed Neural Networks

JITHU J. ATHALATHIL ,¹ MOHAMMED H. TALAFHA ,² AND BHARGAV VAIDYA ,¹

¹*Department of Astronomy, Astrophysics and Space Engineering, Indian Institute of Technology Indore, Indore 453552, India*

²*Research Institute of Science and Engineering, University of Sharjah, 27272, Sharjah, UAE*

ABSTRACT

The solar dynamo relies on the regeneration of the poloidal magnetic field through processes strongly modulated by nonlinear feedbacks such as tilt quenching (TQ) and latitude quenching (LQ). These mechanisms play a decisive role in regulating the buildup of the Sun’s polar field and, in turn, the amplitude of future solar cycles. In this work, we employ Physics-Informed Neural Networks (PINN) to solve the surface flux transport (SFT) equation, embedding physical constraints directly into the neural network framework. By systematically varying transport parameters, we isolate the relative contributions of TQ and LQ to polar dipole buildup. We use the residual dipole moment as a diagnostic for cycle-to-cycle amplification and show that TQ suppression strengthens with increasing diffusivity, while LQ dominates in advection-dominated regimes. The ratio $\Delta D_{\text{LQ}}/\Delta D_{\text{TQ}}$ exhibits a smooth inverse-square dependence on the dynamo effectivity range, refining previous empirical fits with improved accuracy and reduced scatter. The results further reveal that the need for a decay term is not essential for PINN set-up due to the training process. Compared with the traditional 1D SFT model, the PINN framework achieves significantly lower error metrics and more robust recovery of nonlinear trends. Our results suggest that the nonlinear interplay between LQ and TQ can naturally produce alternations between weak and strong cycles, providing a physical explanation for the observed even-odd cycle modulation. These findings demonstrate the potential of PINN as an accurate, efficient, and physically consistent tool for solar cycle prediction.

Keywords: Quiet sun (1322), Solar cycle (1487), Solar dynamo (2001), Sunspot cycle (1650), Neural networks (1933)

1. INTRODUCTION

The solar dynamo is a fundamental process responsible for maintaining the Sun’s magnetic field Parker (1955, 1958). This mechanism operates within the Sun’s interior, particularly in the convection zone, where the interplay of turbulent plasma motions and rotational effects creates and sustains magnetic fields through magnetohydrodynamic (MHD) processes (Tobias 2009; Charbonneau 2014; Sekii & Shibahashi 2015; Charbonneau & Sokoloff 2023). The solar cycle, approximately 11 years long, is characterised by the periodic increase and decrease in the number of sunspots. This cycle is driven by the solar dynamo, which modulates the magnetic field’s strength and polarity over time (Charbonneau 2010; Abreu et al. 2012; Bhowmik et al. 2023). Sunspots are temporary activity on the Sun’s photosphere that appear as spots darker than the surrounding areas. They are regions of intense magnetic activ-

ity, and their cyclic appearance is a direct manifestation of the solar dynamo’s operation, (Charbonneau 2014; Bhowmik et al. 2023; Vasil et al. 2024). The Sun’s equator rotates faster than its poles, creating shear that stretches and twists magnetic field lines, contributing to the generation of the toroidal magnetic field component (Ulrich & Boyden 2005; Choudhuri 2023). This large-scale meridional circulation, together with differential rotation, transports magnetic flux on the solar surface from low latitudes toward the poles and plays a significant role in regulating the solar cycle dynamics (Babcock 1961; Leighton 1969; Choudhuri 2021). The α -effect involves the twisting of magnetic field lines due to helical turbulence, while the ω -effect refers to the shearing of poloidal magnetic fields into toroidal fields by differential rotation (Parker 1955; Steenbeck 1966).

The Surface Flux Transport (SFT) model plays a crucial role in simulating the evolution of solar magnetic fields by describing the transport and redistribution of

magnetic flux on the Sun's surface (Leighton (1964); Wang et al. (1989); Yeates et al. (2023) and references therein). It incorporates various mechanisms such as differential rotation, meridional circulation and supergranular diffusion to describe the transport and evolution of magnetic flux (Cameron et al. 2012; Jiang et al. 2014). The model starts with the emergence of magnetic dipoles and uses the induction equation to track the evolution of the magnetic field, assuming it behaves as if it were purely radial after emergence (Leighton 1964; Jiang et al. 2014).

The formation of the toroidal field from the poloidal field is a linear process. In contrast, the transformation of the toroidal field back into a poloidal field is nonlinear, governed by mechanisms such as tilt quenching (TQ) (Dasi-Espuig et al. 2010; Lemerle & Charbonneau 2017; Karak & Miesch 2017; Karak & Miesch 2018; Jha et al. 2020) and latitude quenching (LQ) (Li et al. 2003; Solanki et al. 2008; Tlatov & Pevtsov 2010; Jiang et al. 2011a; Jiang 2020), which act on the source term implemented within the SFT framework (Charbonneau et al. 2005; Petrovay 2020; Talafha et al. 2022). TQ refers to the tendency of stronger cycles to produce ARs with smaller tilts relative to the equator (Jha et al. 2022), while LQ corresponds to the emergence of ARs at higher latitudes during stronger cycles (Yeates et al. 2025).

These two mechanisms are not the only ones to consider; other attempts were to include surface inflows toward ARs as a nonlinearity to the model (Nagy et al. 2017; Martin-Belda & Cameron 2017; Teweldebirhan et al. 2024; Talafha et al. 2025). All of the possible nonlinearities come with a great value in completing the poloidal-toroidal formation. Nonlinearities like TQ and LQ are essential for the predictability and stability of the solar magnetic activity cycle. They ensure that the solar cycle amplitude remains within a limited range, preventing extreme variations that could disrupt the solar dynamo process, (Deng et al. 2015; Jiang 2020). The nonlinear feedback mechanisms provided by TQ and LQ are critical in the Babcock-Leighton dynamo model. These mechanisms help explain observed long-term solar cycle variability, such as the Gnevyshev-Ohl rule, which describes the alternation of strong and weak solar cycles (Yeates et al. 2025).

Expanding on the methodology of (Jiang et al. 2014), who investigated the asymptotic dipole contribution of ARs depending on their properties (Petrovay et al. 2020) introduced the dynamo effectivity range (λ_R), which quantifies the latitudinal extent over which the surface flows efficiently transport magnetic flux before it is dissipated by diffusion. Dynamo effectivity range plays a crucial role in determining the relative effectiveness of

TQ to LQ, and consequently, λ_R provides a natural scaling parameter for comparing and quantifying the contributions of these nonlinear feedback mechanisms across different dynamo models.

Traditional grid-based numerical models and analytical approaches face several limitations when addressing the nonlinear processes inherent in the solar dynamo. This includes complex nonlinear interactions, such as the coupling between polar magnetic fields and active-region fields (Deng et al. 2015; Shuang et al. 2015).

Physics-Informed Neural Networks (PINN) have emerged as a significant advancement in the intersection of machine learning and physical sciences, offering innovative solutions for complex problems governed by physical laws. PINN incorporate physical laws, often described by partial differential equations (PDEs), directly into the neural network training process. This integration helps in achieving high accuracy even with limited data (Falas et al. 2020; Markidis 2021; Wang et al. 2023). It's known for its ability to solve problems with minimal data, leveraging the underlying physics to guide the learning process. This results in efficient and accurate modelling of physical systems (Falas et al. 2020; Lenz et al. 2024; Song et al. 2024). PINN demonstrate robustness in scenarios with sparse or noisy data by incorporating physical constraints, which helps in maintaining predictive accuracy (Yang & Foster 2022; Li et al. 2024; Zou et al. 2024). PINN are used to solve various PDEs in scientific computing, including fluid dynamics, structural analysis, and turbulence modelling (Markidis 2021; Khalid et al. 2024; Fox et al. 2024). They are employed in modelling complex systems where traditional methods may fall short, such as in the simulation of localised waves and nonlinear Schrödinger equations (Guo et al. 2023).

PINN offer a promising alternative framework for solving the solar SFT problem, particularly in capturing its nonlinear behaviour and enhancing predictive capability. By embedding the governing SFT equations directly into the neural network's loss function, PINN can learn solutions consistent with both physical laws and available magnetic field data. Their mesh-independent formulation ensures better numerical stability and flux conservation, which are crucial for accurately reproducing observed polar field evolution and enhancing solar cycle predictions. While the present work focuses on the physics-constrained implementation, further extensions could incorporate data assimilation and multi-parameter optimisation to refine the representation of nonlinear effects and improve forecasting accuracy (Moschou et al. 2023; Zhang et al. 2024; Gholam-pour et al. 2024; Athalathil et al. 2024).

This work investigates the impact of incorporating nonlinearities of the solar cycle modulation as TQ and LQ in the SFT model using PINN techniques and compares the result with the literature. We further aim to understand the complex interplay between these quenching mechanisms in the buildup of the polar field from one cycle to the next. This article is structured as follows: Section 2 describes the SFT model and implementation using PINN, highlighting the source model and nonlinearities adopted in this study. In section 3, we explain how including the nonlinearities affected the model. Section 4 compares the results of PINN and a simple upwind scheme used in (Petrovay & Talafha 2019) and (Talafha et al. 2022) to solve the SFT equation. Section 5 presents an interpretation from this study on the variation of solar cycle, and section 6 concludes the study.

2. SFT - PINN FRAMEWORK

2.1. SFT Model

In this work, we simulate a 1D SFT model within a Babcock–Leighton–type dynamo framework, as described in (Talafha et al. 2022). SFT equation (Eq. 1) is a transport equation for the radial magnetic field derived from the induction equation. The decay term was included later to address the problem of abrupt drift in the polar field over time. This issue arises when fluctuations in cycle amplitude lead to a random walk of the unsigned solar dipole moment from one cycle to the next, eventually reaching values far exceeding the typical total contribution of ARs in a cycle (Schrijver et al. 2002)

$$\frac{\partial B}{\partial t} = \frac{1}{R \cos \lambda} \frac{\partial}{\partial \lambda} (B u \cos \lambda) + \frac{\eta}{R^2 \cos \lambda} \frac{\partial}{\partial \lambda} \left(\cos \lambda \frac{\partial B}{\partial \lambda} \right) - \frac{B}{\tau} + S(\lambda, t) \quad (1)$$

where R is the solar radius, u is the meridional flow, η is the diffusivity and τ represent the decay time. The source term $S(\lambda, t)$ represents the a parametrised source function describing the spatio-temporal emergence of p- and f-polarities on the solar surface as described in (Petrovay & Talafha 2019). In their work, the source is represented as a pair of rings of opposite magnetic polarity as:

$$\begin{aligned} S(\lambda, t) = & k A_m f_{sph} S_1(t) S_2 [\lambda; \lambda_0(t) - \Delta\lambda(t), \delta\lambda] \\ & - k A_m S_1(t) S_2 [\lambda; \lambda_0(t) + \Delta\lambda(t), \delta\lambda] \\ & + k A_m S_1(t) S_2 [\lambda; -\lambda_0(t) - \Delta\lambda(t), \delta\lambda] \\ & - k A_m f_{sph} S_1(t) S_2 [\lambda; -\lambda_0(t) + \Delta\lambda(t), \delta\lambda] \end{aligned} \quad (2)$$

where $k = \pm 1$ is a factor alternating between even and odd cycles. A_m is an arbitrary amplitude depending on the flow profile (0.015 for a simple sinusoidal profile) used to ensure that the resulting polar field amplitude roughly agrees with observations. Care was taken to ensure zero net flux on the spherical surface by reducing the amplitude of the equatorward member of each pair by an appropriate sphericity factor f_{sph} .

$S_1(t)$ is the time profile of solar activity in a typical cycle was determined by Hathaway et al. (1994) from the average of many cycles as

$$S_1(t) = a t_c^3 / [\exp(t_c^2/b^2) - c] \quad (3)$$

with $a = 0.00185$, $b = 48.7$, $c = 0.71$, where t_c is the time since the last cycle minimum.

$S_2 [\lambda; \lambda_0(t), \delta\lambda]$ is the latitudinal profile represented by a Gaussian with a fixed full width at half-maximum of $2\delta\lambda = 6.26^\circ$, migrating equatorward during the course of a cycle:

$$S_2(\lambda; \lambda_0, \delta\lambda) = \frac{\delta\lambda_0}{\delta\lambda} \exp [-(\lambda - \lambda_0)^2 / 2\delta\lambda^2] \quad (4)$$

while its standard deviation ($\delta\lambda$) follow the empirical results of Jiang et al. (2011):

$$\delta\lambda = [0.14 + 1.05(t/P) - 0.78(t/P)^2] \lambda_0 \quad (5)$$

where P is the cycle period (11 years). The latitudinal separation of the rings is a consequence of Joy’s law:

$$2\Delta\lambda = 0.5 \frac{\sin \lambda}{\sin 20^\circ} \quad (6)$$

while the mean latitude λ_0 of activity during the course of a cycle at a given phase of cycle i , is given by a quadratic fit derived by Jiang et al. (2011b) from many observed solar cycles:

$$\lambda_0(t, i) = 26.4 - 34.2(t/P) + 16.1(t/P)^2 \quad (7)$$

and if it is parametrised as a function of cycle strength, it represents the LQ nonlinearity, Talafha et al. (2022):

$$\lambda_0(t, i) = [26.4 - 34.2(t/P) + 16.1(t/P)^2] \times \left(1 + \frac{b_{\text{lat}}}{14.6} \left(\frac{A_n}{A_0} - 1 \right) \right) \quad (8)$$

With b_{lat} determining the rate at which the emergence latitude increases and is set to 2.4 based on (Jiang et al. 2011), (A_n/A_0) denotes the strength of a given cycle relative to a reference cycle. We model fluctuations as multiplicative noise acting on the amplitude of the poloidal field source. Hence, the cycle amplitude follows a log-normal distribution described as $A_n = A_0 \times 10^G$, where

G is a Gaussian random variable with zero mean and standard deviation 0.13. The normalization constant is set to $A_0 = 0.001 e^{7/\tau}$ (Gauss) which yields dipole moment values comparable to observations.

TQ is introduced by multiplying the nominal Joy's law tilt with a suppression factor that scales with cycle amplitude:

$$\Delta\lambda = \delta_0 \sin \lambda_{LQ} \left(1 - b_{\text{joy}} \left(\frac{A_n}{A_0} - 1 \right) \right) \quad (9)$$

Where $\delta_0 = 1.5$ is the Joy's law amplitude coefficient, and the constant coefficient $b_{\text{joy}} = 0.15$ specifies the quenching efficiency. Together, TQ and LQ act to suppress the buildup of the large-scale dipole. While TQ limits the separation of opposite polarities within emerging ARs, LQ reduces the efficiency of flux cancellation across the equator.

According to Petrovay et al. (2020), the dynamo effectiveness range, λ_R , characterises the competition between advective transport by the meridional flow and diffusive transport due to turbulent mixing in the surface magnetic flux evolution. It is defined as

$$\lambda_R = \sqrt{\frac{\eta}{u_0 R}}. \quad (10)$$

where u_0 is the characteristic meridional flow amplitude. This parameter plays a central role in determining the relative impact of LQ and TQ on the cycle-integrated dipole moment, as discussed in Talafha et al. (2022). In particular, the ratio of their respective deviation scales as

$$\Delta_{LQ}/\Delta_{TQ} \sim C_1(\bar{\lambda}_0) + C_2(\bar{\lambda}_0)/\lambda_R^2 \quad (11)$$

where Δ_{LQ} and Δ_{TQ} denote the deviations in the net contribution of a cycle to the dipole moment from the no quenching case, arising from LQ and TQ, respectively.

The net contribution of each cycle to the buildup of the large-scale dipole is defined as the residual dipole moment:

$$D_{\text{res}}(P, \tau) = D(t) - e^{-P/\tau} D_{\text{cycle min}} \quad (12)$$

where $D(t)$ is the instantaneous dipole moment, $D_{\text{cycle min}}$ is the value at the preceding cycle minimum. This formulation removes the exponential memory of earlier cycles, allowing us to quantify the effective dipole amplification within a single cycle. We use $D_{\text{res}}(P, \tau)$ as a diagnostic throughout this study to compare the influence of TQ versus LQ.

2.2. PINN

The input layer of the PINN model consists of latitude (λ) and time (t), while the output predicts the

magnetic field $B(\lambda, t)$. A brief description of the model is provided below, with a detailed explanation available in our previous work (Athalathil et al. 2024).

For each training point (λ, t) , the network predicts the magnetic field $B_{\text{pinn}}(\lambda, t)$. The derivatives required by the SFT equation are computed using automatic differentiation. Since the network outputs are linked to the inputs through activation functions with known analytical derivatives, derivatives of $B_{\text{pinn}}(\lambda, t)$ with respect to (λ, t) can be evaluated directly using the chain rule. This grid-free approach enables derivative evaluation at any point within the domain and avoids explicit discretisation of both spatial and temporal coordinates.

The loss function is constructed by enforcing the governing SFT equation together with the prescribed initial and boundary conditions at the training points. The neural network weights are then updated via backpropagation to minimize the loss. This iterative optimization continues until the loss converges. We employ a two-step optimisation strategy to train the model. Initially, the ADAM optimiser (Kingma & Ba 2014) is used to achieve rapid convergence in the early stages of training. Subsequently, the L-BFGS optimiser (Liu & Nocedal 1989) is applied to fine-tune the solution and achieve higher precision in the final optimisation.

The loss function for the learning process is constructed as a weighted sum of three components: initial condition loss, boundary condition loss, and PDE residual loss. These components collectively ensure that the PINN solution adheres to the specified initial conditions, satisfies the prescribed boundary conditions, and minimises the residual of the governing partial differential equation (PDE). Mathematically, the loss function is expressed as:

$$\xi = w_{\text{ic}}\xi_{\text{ic}} + w_{\text{bc}}\xi_{\text{bc}} + w_{\text{pde}}\xi_{\text{pde}} \quad (13)$$

Here, the weights w_{ic} , w_{bc} , and w_{pde} balance the contributions of each component to the total loss. This formulation ensures that the model learns a solution consistent with both the physical constraints and the observed data. The components of the loss function ξ_{ic} , ξ_{bc} and ξ_{pde} correspond to the initial condition loss, boundary condition loss, and PDE residual loss, respectively. These components are mathematically defined as:

$$\xi_{\text{ic}} = \frac{1}{N_{\text{ic}}} \sum_{i=1}^{N_{\text{ic}}} \left| B_{\text{pinn}}(\lambda^i, t=0) - B_{\text{init}}(\lambda^i) \right|^2 \quad (14)$$

$$\xi_{\text{bc}} = \frac{1}{N_{\text{bc}}} \sum_{j=1}^{N_{\text{bc}}} \left| B_{\text{pinn}}(\lambda_{\text{bc}}^j, t^j) - B_{\text{bc}}(\lambda_{\text{bc}}^j, t^j) \right|^2 \quad (15)$$

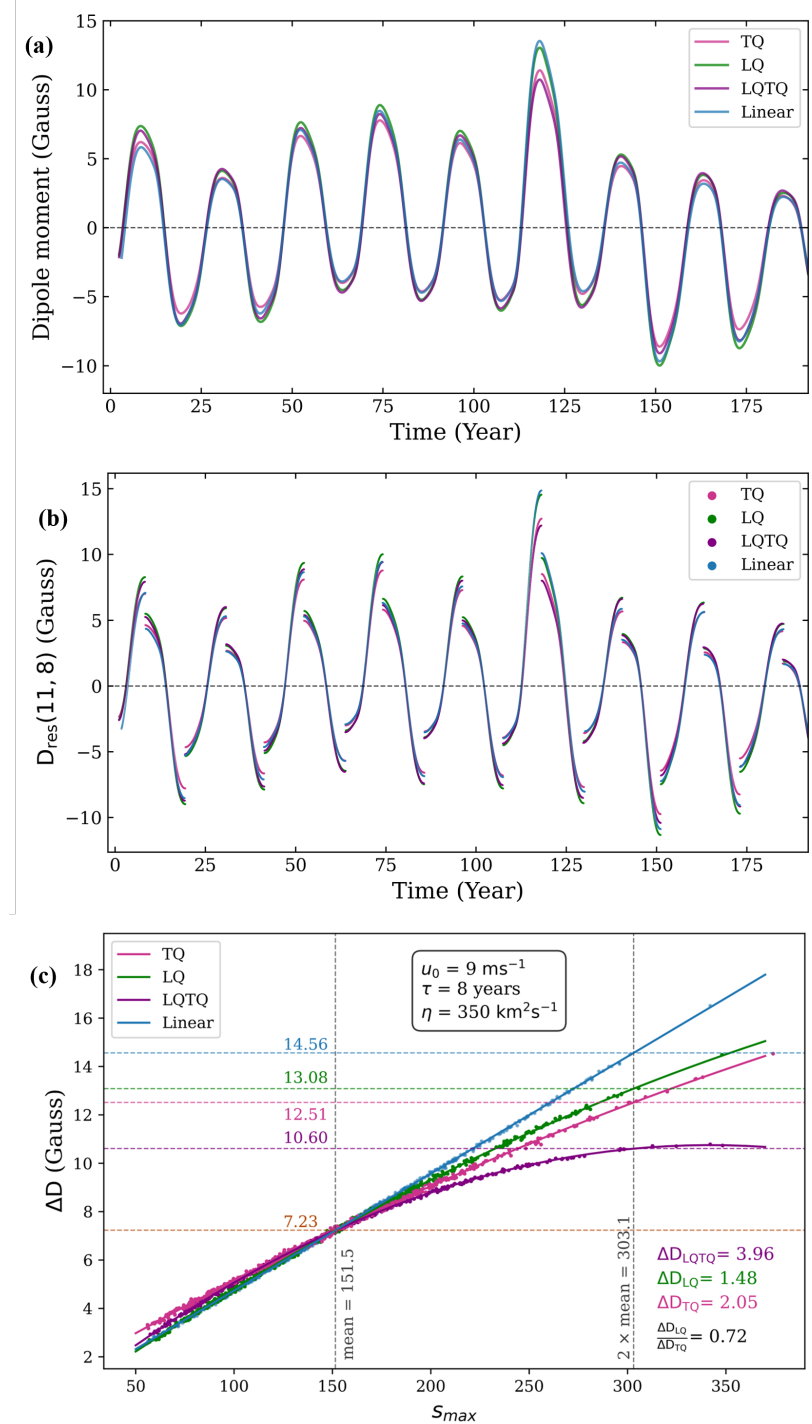


Figure 1. Simulation results for SFT parameters $u_0 = 9 \text{ m/s}$, $\tau = 8 \text{ years}$, and $\eta = 350 \text{ km}^2/\text{s}$. (a) Dipole moment distribution in Gauss across latitudes for each time step over 15 cycles. (b) Time evolution of the residual dipole moment, $D_{\text{res}}(P = 11, \tau = 8)$ (c) Change in dipole moment of each cycle from the previous cycle for different processes (TQ, LQ, LQ+TQ, and linear). Deviations are quantified at twice the mean of the maximum source.

where $f(\lambda, t)$ is the residual function that represents the error in satisfying the SFT equation as given below

$$\xi_{\text{pde}} = \frac{1}{N_{\text{pde}}} \sum_{k=1}^{N_{\text{pde}}} |f(\lambda^k, t^k)|^2 \quad (16)$$

$$\begin{aligned}
f(\lambda, t) = & \frac{\partial B_{\text{pinn}}}{\partial t} - \frac{1}{R \cos \lambda} \frac{\partial}{\partial \lambda} (B_{\text{pinn}} u(\lambda) \cos(\lambda)) \\
& - \frac{\eta}{R^2 \cos \lambda} \frac{\partial}{\partial \lambda} \left(\cos \lambda \frac{\partial B_{\text{pinn}}}{\partial \lambda} \right) + \frac{B_{\text{pinn}}}{\tau} \\
& - S(\lambda, t)
\end{aligned} \quad (17)$$

Here, $B_{\text{pinn}}(\lambda, t)$ represents the predicted magnetic field at each point (λ, t) . The terms N_{ic} , N_{bc} , N_{pde} denote the number of training points used for the initial condition, boundary condition, and domain residual calculations, respectively. $B_{\text{init}}(\lambda)$ is the initial condition (at $t = 0$), while $B_{\text{bc}}(\lambda_{\text{bc}}, t)$ represents the boundary conditions at boundary λ_{bc} . The initial condition is taken to be a dipolar field $B_{\text{init}}(\lambda) \equiv \sin \lambda$. Due to the presence of the decay term in the SFT equation, this dipolar initial magnetic field gets decayed within a few years. To ensure that the choice of initial condition does not influence the final results, we discard the first two solar cycles (22 years) from all simulations and base our analysis only on the subsequent evolution. Neumann boundary conditions with zero gradient are imposed at the latitudinal boundaries, allowing unimpeded poleward transport of magnetic flux consistent with the SFT model.

3. RESULTS

A comprehensive parameter study was carried out by systematically varying the SFT parameters, through four different cases: No quenching case (linear), TQ, LQ and the combination of both LQ and TQ (LQTQ). The results corresponding to $u_0 = 9 \text{ ms}^{-1}$, $\tau = 8 \text{ years}$, and $\eta = 350 \text{ km}^2 \text{s}^{-1}$ are presented as an example.

Figure 1(a) shows the time evolution of the axial dipole moment in Gauss. During weaker cycles, all models exhibit similar dipole amplitudes. However, during the strong cycle, TQ reduces the mean Joy's-law tilt, increasing cancellation between opposite polarities within a hemisphere, while LQ shifts flux emergence poleward, reducing cross-equatorial transport. Acting together, these effects substantially suppress the net polar dipole buildup, producing the prominent deviation seen around year ~ 120 . The combined LQTQ model consistently yields the lowest dipole amplitudes, reflecting the combined regulatory effects of both feedback mechanisms. The overall magnetic dipole moment shown in Figure 1(a) also has a contribution from the preceding cycles. These cumulative contributions from prior cycles need to be removed to accurately capture the net build-up of the dipole moment within each solar cycle. Figure 1(b) shows the time evolution of the residual dipole moment D_{res} , as defined in equation 12.

This diagnostic isolates cycle-to-cycle amplification and reveals Gaussian-like growth curves for each solar cycle, with their peaks indicating the rate of dipole amplification. The plot shows that while all simulated SFT models exhibit similar overall temporal patterns, subtle differences arise in the amplitude and shape of individual cycles due to the influence of the quenching mechanisms.

The gain of the dipole moment per cycle represents the net accumulation of the polar magnetic field throughout a cycle. We calculated the gain (ΔD) as the residual dipole moment at the end of each cycle (n) at the mean and twice the mean of the maximum source amplitude injected during the cycle (S_{max}, n) which serves as a ballpark for the strength of the given cycle. The variation of ΔD as a function of the S_{max}, n of the cycle is shown in Figure 1(c). The linear case is used as a reference to understand the effect of quenching. In the linear regime, ΔD (and hence the dipole moment gain) increases proportionally with the source amplitude. The inclusion of TQ and LQ introduces significant nonlinear saturation, particularly at higher source strengths. The combined effect (LQTQ) shows the strongest suppression, resulting in the lowest ΔD values. For lower amplitude cycles, the nonlinear cases can produce slightly enhanced dipole moment gains relative to the linear case.

We calculate the deviations due to different quenching mechanisms (ΔD_{LQ} , ΔD_{TQ} , ΔD_{LQTQ}) as the change in ΔD evaluated from the linear case at twice the mean of $S_{\text{max}, n}$. The deviation in dipole moment due to the combined nonlinearities ($\Delta D_{\text{LQTQ}} = 3.96$) is larger than that from either mechanism alone ($\Delta D_{\text{TQ}} = 2.04$ for tilt quenching and $\Delta D_{\text{LQ}} = 1.48$ for latitude quenching). The resulting ratio $\Delta D_{\text{LQ}}/\Delta D_{\text{TQ}} = 0.72$ indicates that TQ is the more effective mechanism in suppressing the polar dipole moment, while LQ provides a secondary but reinforcing contribution for the chosen set of SFT parameters. These results complement previous findings by [Talafha et al. \(2022\)](#).

Figure 2 presents the parameter sensitivity of the nonlinear quenching effects, showing the variations of ΔD_{LQ} , ΔD_{TQ} , and their ratio $\Delta D_{\text{LQ}}/\Delta D_{\text{TQ}}$ across the SFT parameter space. Panels (a)–(f) show the two-dimensional sensitivity maps of ΔD_{LQ} , ΔD_{TQ} , and their ratio in the (u_0, η) parameter space for $\tau = 8 \text{ yr}$ (left column) and $\tau = \infty$ (right column). Warmer colours (dark orange to red) represent larger deviations of ΔD_{LQ} , indicating stronger suppression of the dipole moment in diffusion-dominated regimes, whereas cooler tones (blue to cyan) correspond to weaker suppression. In contrast, ΔD_{TQ} varies less systematically but remains more pronounced in advection-dominated regimes (high u_0 , low η). The ratio map reveals that $\Delta D_{\text{LQ}}/\Delta D_{\text{TQ}}$ is

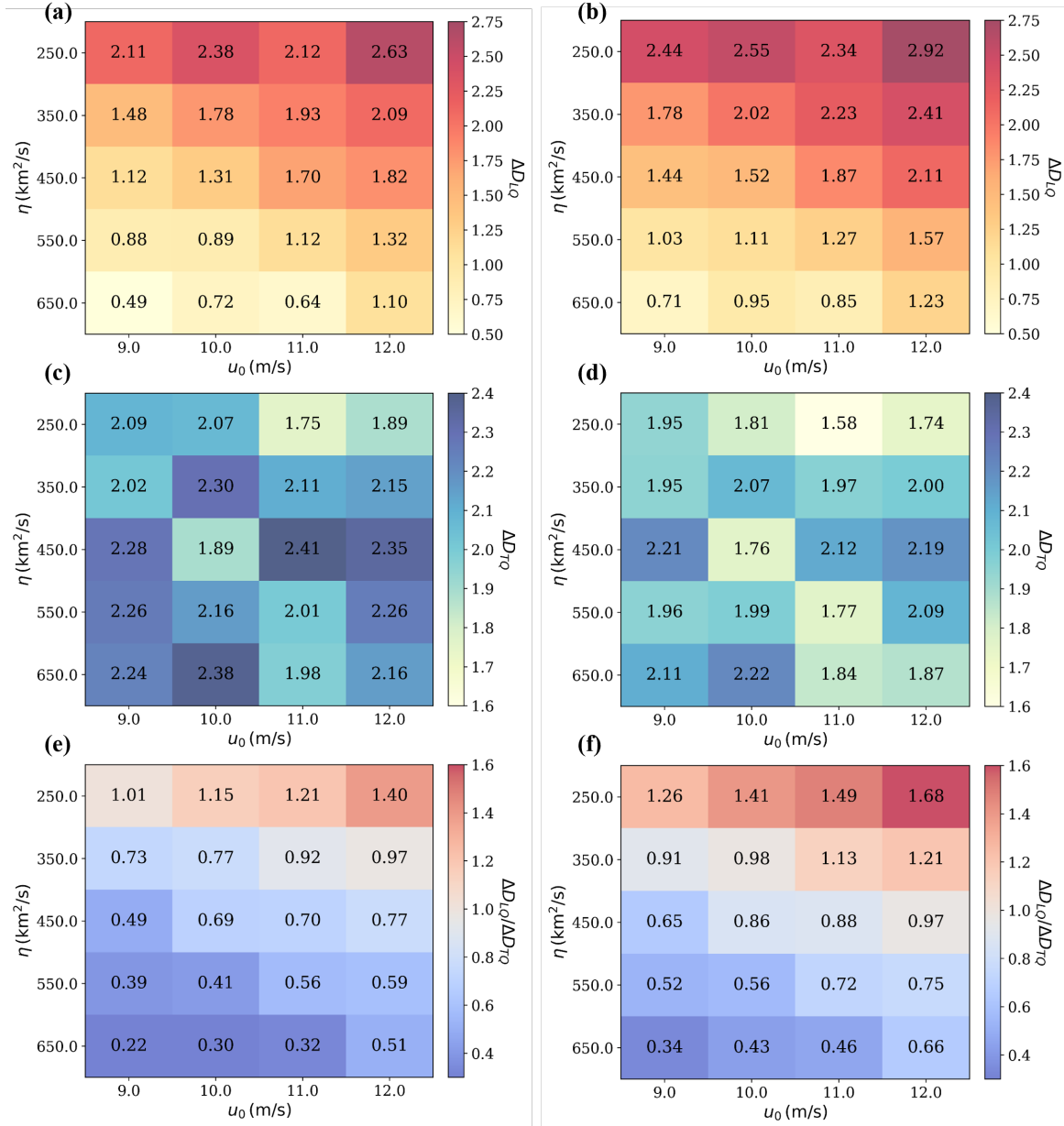


Figure 2. Parameter sensitivity of the nonlinear quenching effects across the SFT parameter space. Panels (a), (c), (e) and (b), (d), (f) show the sensitivity maps of ΔD_{LQ} , ΔD_{TQ} , and their ratio across the (u_0, η) parameter space for $\tau = 8$ and $\tau = \infty$, respectively.

largest at low diffusivity and high flow speed, gradually declining as η increases. Together, these results confirm that LQ dominates in advection-dominated regions, whereas TQ becomes increasingly effective in diffusion-dominated regimes. The ΔD_{LQ} and ΔD_{TQ} for different SFT parameters are presented in Table 1.

A comparative analysis of the ratio $\Delta D_{LQ}/\Delta D_{TQ}$ as a function of λ_R is shown in Figure 3 for two decay timescales: $\tau = 8$ [yr] and $\tau = \infty$, respectively. The green and magenta shaded regions mark the LQ-dominated and TQ-dominated regimes, respectively. In

both panels, the teal points correspond to the PINN results, while the crimson markers show the values from [Talalha et al. \(2022\)](#). With increasing λ_R , LQ becomes progressively less influential compared to TQ. This behaviour is particularly evident at higher values of λ_R , where the contribution of TQ increasingly dominates the modulation of the dipole moment, and in turn the strength of the next cycle. A nonlinear fit of the form $C_1 + C_2/\lambda_R^2$ is applied to the PINN data, yielding best-fit (indicated by the dashed black curve in Figure 3). The best fit values are found to be $C_1 = -0.3847$ and

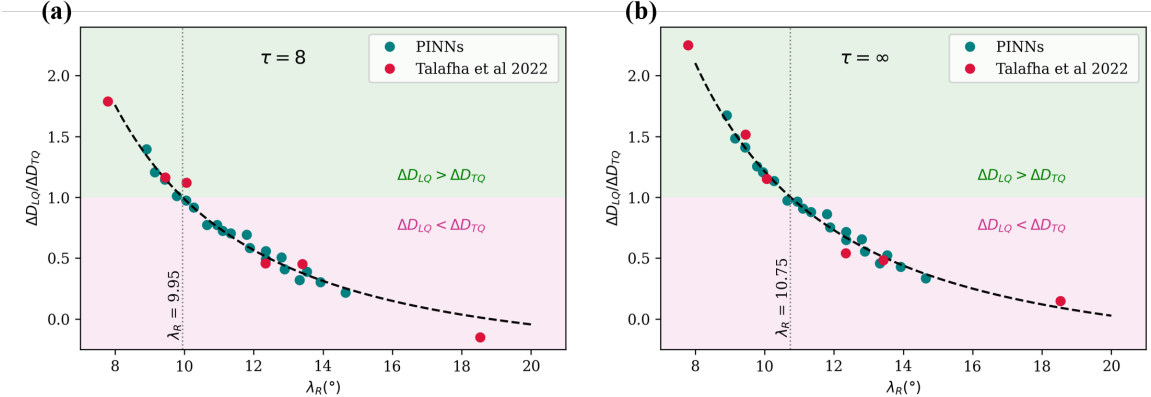


Figure 3. Relative importance of nonlinear quenching mechanisms. Ratio $\Delta D_{LQ}/\Delta D_{TQ}$ is plotted as a function of the dynamo effectivity range λ_R for finite $\tau = 8$ (a) and $\tau = \infty$ (b). The teal symbols show the PINN results, the dashed black curve is the best-fit inverse-square law ($C_1 + C_2/\lambda_R^2$), and the crimson points are values from [Talafha et al. \(2022\)](#). Best-fit parameters: $C_1 = -0.3847$, $C_2 = 136.86$ ($\tau = 8$); $C_1 = -0.3679$, $C_2 = 158.19$ ($\tau = \infty$). The shaded regions highlight regimes dominated by LQ (green) and TQ (magenta), showing that LQ dominates at low λ_R (advection-dominated regimes) and TQ becomes increasingly effective at higher λ_R (diffusion-dominated regimes).

$C_2 = 136.8595$ ($\tau = 8$ [yr]). For a comparison of the fitted parameters and a detailed mathematical interpretation of the corresponding formula, see [Talafha \(2025\)](#). The PINN data exhibit a smooth and consistent trend that closely follows the expected inverse square dependence as compared to the values in ([Talafha et al. 2022](#)). A detailed comparison is presented in Section 4, highlighting the improved reliability and reduced variance in the PINN-based results, reinforcing the accuracy and robustness of the PINN framework in capturing the underlying physical behaviour of the system.

4. IMPROVED ACCURACY WITH PINN

The improved agreement of the PINN model with the expected inverse square behaviour, as observed in Figure 3 (a) and (b), motivates a deeper evaluation of its quantitative performance. Table 2 presents a comparative analysis of the dipole moment predictions from our PINN-based approach and the numerical scheme by ([Talafha et al. 2022](#)) using standard performance metrics. The comparison is performed between the model-predicted $\Delta D_{LQ}/\Delta D_{TQ}$ values and their corresponding fitted profiles to assess the scatter and to evaluate how well the underlying nonlinear trend is captured. The definitions of the error metrics, along with their distributions, are provided in Appendix A. The Mean Absolute Error (MAE), Mean Squared Error (MSE), and Root Mean Squared Error (RMSE) values are significantly lower for the PINN model, indicating better overall predictive accuracy. The distribution for these error metrics have low scatter for PINNs (see Figure 5) thus indicating improved model performance.

With a coefficient of determination (R^2) score of 0.9841, PINN model exhibits an even closer match to

the best fit profile, improving upon the 0.9730 achieved in ([Talafha et al. 2022](#)). The maximum error and Mean Absolute Percentage Error (MAPE) are also considerably reduced in the PINN case, highlighting the model's robustness across the entire range of inputs. These results suggest that the PINN framework offers improved accuracy and reliability for modelling nonlinear quenching effects. Unlike traditional schemes that may suffer from numerical sensitivity to the resolution of the simulation box, PINN naturally incorporate physical constraints and exhibits greater stability across the dynamo parameter space.

In terms of computational efficiency, each PINN run (training on a single set of SFT parameters) typically required \sim 1-2 hours on a standard CPU node (Intel i7, 4 cores), or about 15-20 minutes on a single GPU (NVIDIA V100). In comparison, the traditional upwind finite-difference scheme completes within a few minutes on the same CPU, but suffers from greater numerical scatter and resolution sensitivity. Thus, while PINN incurs a higher per-run training cost, it yields smoother and more accurate solutions across the parameter space, particularly in the nonlinear regimes of interest.

Although re-tuning the hyperparameters is not necessary in the PINN architecture, the model must be retrained whenever the initial conditions or simulation parameters are altered ([Athalathil et al. 2024](#)). In the context of the present work, retraining is required each time the SFT parameters (u_0 , η and τ) are modified. This repeated retraining increases the overall computational cost and partially offsets the efficiency gains expected from machine learning approaches. Recent developments, such as neural operators including the Fourier Neural Operator and its physics-informed vari-

Table 1. Comparison of dipole moment deviations ΔD_{LQ} and ΔD_{TQ} for different values of u_0 and η . The ratio quantifies the relative importance of the two quenching mechanisms for finite $\tau = 8$ and $\tau \rightarrow \infty$. Transition values ($\Delta D_{\text{LQ}}/\Delta D_{\text{TQ}} \approx 1$) are shown in bold.

u_0 (m/s)	η (km ² /s)	λ_R (°)	$\tau = 8$			$\tau = \infty$		
			ΔD_{LQ}	ΔD_{TQ}	$\Delta D_{\text{LQ}}/\Delta D_{\text{TQ}}$	ΔD_{LQ}	ΔD_{TQ}	$\Delta D_{\text{LQ}}/\Delta D_{\text{TQ}}$
9	250	9.78	2.11	2.09	1.01	2.44	1.95	1.25
10	250	9.44	2.38	2.07	1.15	2.55	1.81	1.41
11	250	9.15	2.12	1.75	1.21	2.34	1.57	1.49
12	250	8.91	2.63	1.89	1.40	2.92	1.74	1.68
9	350	11.10	1.48	2.04	0.72	1.78	1.95	0.91
10	350	10.65	1.78	2.30	0.77	2.02	2.07	0.98
11	350	10.27	1.93	2.11	0.92	2.23	1.97	1.13
12	350	9.95	2.09	2.15	0.97	2.41	2.00	1.21
9	450	12.35	1.12	2.28	0.49	1.44	2.21	0.65
10	450	11.79	1.31	1.89	0.69	1.52	1.76	0.86
11	450	11.33	1.70	2.41	0.70	1.87	2.12	0.88
12	450	10.94	1.82	2.35	0.77	2.11	2.19	0.97
9	550	13.53	0.88	2.26	0.39	1.03	1.96	0.52
10	550	12.89	0.89	2.16	0.41	1.11	1.99	0.56
11	550	12.35	1.12	2.00	0.56	1.27	1.76	0.72
12	550	11.89	1.32	2.26	0.58	1.57	2.09	0.75
9	650	14.65	0.48	2.24	0.22	0.71	2.11	0.34
10	650	13.93	0.72	2.38	0.30	0.95	2.22	0.43
11	650	13.32	0.64	1.98	0.32	0.84	1.84	0.46
12	650	12.80	1.10	2.16	0.51	1.23	1.87	0.65

Metric	PINN	(Talafha et al. 2022)
MAE	0.032293	0.090180
MSE	0.001588	0.010587
RMSE	0.039855	0.102894
R^2	0.984119	0.972994
Max Error	0.093414	0.158281
MAPE (%)	6.017877	23.306108

Table 2. Comparison of error and fit metrics between PINN model and (Talafha et al. 2022) for $\tau = 8$. Details of the metric calculation are given in Appendix A

ants (Li et al. 2020; Kovachki et al. 2021; Li et al. 2021; Zhong & Meidani 2025) have shown potential in addressing this retraining bottleneck. Similarly, reduced-order surrogate modelling approaches (Conti et al. 2024) and parameter-conditioning strategies (Chen et al. 2022; Madhavan et al. 2024) aim to enhance adaptability across parameter spaces. Together, these methods offer promising routes toward minimising the need for repeated training and improving computational efficiency.

5. DISCUSSION

Through this work, we explored the SFT parameter space to understand the role of quenching mechanisms in dipole moment buildup in a Babcock-Leighton type solar dynamo. Using the PINN framework, we independently verified the inverse relationship between dipole moment gain and the dynamo effectivity range λ_R , previously reported in (Talafha et al. 2022). The ratio $\Delta D_{\text{LQ}}/\Delta D_{\text{TQ}}$ derived from PINN follows a smooth inverse-square trend, accurately captured by the empirical relation $C_1 + C_2/\lambda_R^2$, as shown in Figure 3.

The PINN framework successfully recovers the observed trend and further refines the empirical fit by enforcing physical consistency, leading to tighter constraints on the governing coefficients. This establishes PINN as a powerful tool for both prediction and insight in solar dynamo modelling. In our subsequent paper, we will use this model to predict the next solar cycle by training the neural network on WSO synoptic maps.

We found that the efficiency of nonlinear quenching mechanisms is inherently dependent on the underlying transport regime. The ratio $\Delta D_{\text{LQ}}/\Delta D_{\text{TQ}}$ serves as a

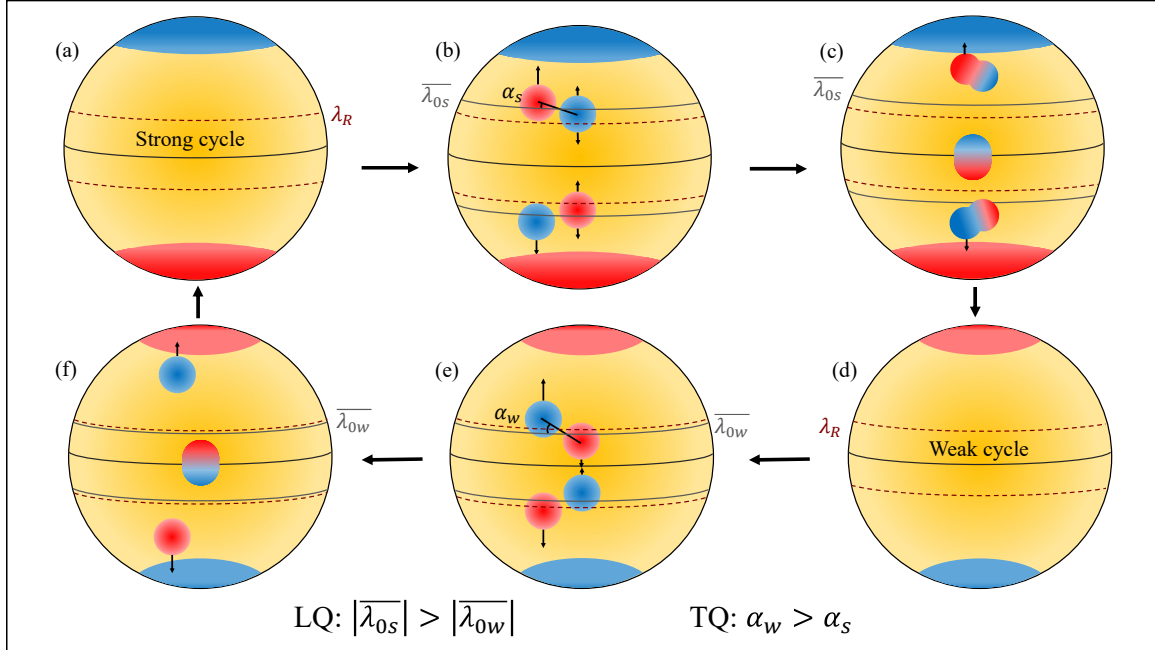


Figure 4. Schematic illustration of the roles of latitude quenching (LQ) and tilt quenching (TQ) in regulating solar cycle strength. Panels (a–c): strong-cycle scenario. (a) Due to TQ, the mean tilt angle of emerging BMRs decreases from α_w (weak cycle) to α_s (strong cycle), enhancing flux cancellation between trailing and leading polarities. (b) LQ simultaneously shifts the mean emergence latitude poleward from $\bar{\lambda}_{0w}$ to $\bar{\lambda}_{0s}$, reducing cross-equatorial cancellation. (c) The combined effect decreases poleward transport of flux, leaving a weaker polar field and reducing the amplitude of the subsequent cycle (d). Panels (e–f): weak-cycle scenario. (e) With weaker TQ, BMRs retain larger Joy’s-law tilts, while LQ shifts the mean emergence latitude equatorward, enhancing cross-equatorial cancellation. (f) This facilitates stronger poleward transport of trailing flux, yielding an enhanced polar field that seeds a stronger following cycle (a). Together, these processes illustrate how the interplay of LQ and TQ can produce cycle-to-cycle modulation consistent with the Gnevyshev–Ohl rule and the observed even–odd alternation in solar activity.

diagnostic indicator of this behaviour, and its variation with λ_R reveals a distinct transition in dominance between the two mechanisms. Particularly, the point at which the ratio crosses unity (i.e., $\Delta D_{LQ}/\Delta D_{TQ} = 1$) represents a critical threshold beyond which TQ becomes the dominant nonlinear feedback, replacing LQ. This transition typically occurs around $\lambda_R \approx 10^\circ$ (9.95° for $\tau = 8$ and 10.75° for $\tau = \infty$), suggesting that TQ is more effective in advection-dominated regimes (low λ_R), whereas LQ becomes increasingly significant in diffusion-dominated regimes (high λ_R). This agrees with the findings of (Talafha et al. 2025), where $\lambda_R \approx 10.5^\circ$ was obtained in SFT simulations without surface inflows toward ARs. The sharp decline in the ratio with increasing λ_R highlights a physical bifurcation in the solar

dynamo’s nonlinear response depending on the relative strength of transport processes. Models incorporating LQ show a broad range of contributions to the modulation of solar cycles, from insignificant to dominant (Jiang 2023). However, (Yeates et al. 2025) found that, using historical data and SFT models, LQ has a stronger evidence base compared to TQ.

We notice the nonlinearities have negligible dependence on the choice of τ as illustrated in Figure 3. This can be understood from the order of magnitude scaling form of the SFT equation:

$$\frac{RB}{tu_0} \simeq \frac{B}{\lambda} + \left(\frac{\lambda_R}{\lambda} \right)^2 B - \frac{BR}{\tau u_0} + \frac{SR}{u_0}, \quad (18)$$

Where the left-hand side is the characteristic temporal term and the terms on the right-hand side repre-

sent, respectively, advection, diffusion, radial decay, and source contributions (see Appendix B for derivation). Comparing the diffusion and decay terms, it becomes clear that the decay term is insignificant under realistic solar conditions. For typical surface diffusivity values ($\eta \approx 500 \text{ km}^2 \text{s}^{-1}$), the decay timescale τ would need to be of the order of a few years or less to match the strength of the diffusive term. Such a small value is physically unrealistic, confirming that decay is not an efficient method for limiting the polar dipole moment when using PINN modulation. The PINN architecture enforces global smoothness during training, introducing an implicit decay-like regularization. This implicit effect naturally stabilizes the field without explicit exponential decay. This implies that the SFT solution is more dependent on λ_R compared to τ . Hence, nonlinearities such as TQ and LQ are more effective in regulating the polar dipole moment than the decay term.

Previous studies have explored the effect of nonlinearities on the solar dynamo; however, a clear physical interplay of the quenching mechanisms has not been discussed. We present a possible underlying physical operation of LQ and TQ in regulating the solar dipole moment for a given value of λ_R , schematically illustrated in Figure 4. During a strong cycle (see Figure 4(a)), due to TQ, the mean tilt angle of emerging BMRs reduces from its nominal value α_w (in weak cycles) to a lower value α_s . This reduction enhances the possibility of flux cancellation between the trailing and leading opposite polarities. At the same time, LQ shifts the mean emergence latitude of BMRs from a lower value $\bar{\lambda}_{0w}$ (in weak cycles) to a higher value $\bar{\lambda}_{0s}$, pushing them farther away from the equator. λ_R defines the equatorward limit of flux emergence that can be efficiently advected to the poles before diffusive decay dominates; consequently, BMRs emerging above this threshold experience longer diffusive timescales and weaker effective diffusion. As a result, cross-equatorial flux cancellation decreases once BMRs begin to emerge above λ_R (see Figure 4(b)). The combined effect of changing tilt angle and mean emergence latitude due to TQ and LQ, respectively, there in a considerable increase in the flux cancellation between the leading and trailing polarities in a hemisphere. Consequently, the amount of magnetic flux transported toward the poles is decreased. This suppression of poleward flux transport significantly reduces the efficiency of poloidal field generation during strong cycles (see Figure 4(c)). As a result, stronger cycles contribute less effectively to the buildup of the dipole moment, ultimately leaving behind a weaker polar field and giving rise to a weaker subsequent cycle (Figure 4(d)).

In weak cycles, BMRs emerge with typical Joy's law tilts (α_w), as TQ is weak, which lowers the probability of flux cancellation between the leading and trailing polarities. Simultaneously, LQ shifts the mean emergence latitude equatorward to $\bar{\lambda}_{0w}$, placing it below λ_R where diffusive losses are more significant. Such a shift, further aided by surface inflows toward ARs (Talafha et al. 2025), enhances cross-equatorial flux cancellation (see Figure 4(e)). The combined effect results in less flux cancellation between the leading and trailing polarities within a hemisphere. As a result, the trailing polarity moves toward the poles, leading to a stronger polar field (see Figure 4(f)). The enhanced axial dipole at the end of a weak cycle then provides a stronger poloidal seed for the subsequent cycle, which in turn typically generates a stronger toroidal field and, consequently, a stronger solar cycle (Figure 4(a)). This is consistent with Gnevyshev-Ohl Rule as discussed by (Charbonneau et al. 2007; Nagovitsyn et al. 2024). This regulatory feedback is fundamental to the long-term stability of the solar cycle as it prevents the Sun from entering a state of unbounded cycle amplitude growth and promotes recovery from periods of very low activity.

The nonlinear feedback mechanism naturally implies an alternation between weak and strong solar cycles (i.e., an even-odd cycle pattern). However, such a perfect odd–even alternation in the actual solar cycle record has not been observed regularly. The classical expectation of an odd–even alternation rests on the simplifying assumption that the dynamo parameters remain constant over time. In reality, these parameters, particularly the dimensionless quantity λ_R , vary from cycle to cycle due to fluctuations in the meridional flow speed (u_0) and magnetic diffusivity (η). Consequently, the influence of LQ and TQ also changes between cycles. As a result, the system departs from the strict periodicity implied by the constant parameter scenario, producing the irregular sequence of strong and weak cycles as observed. This cycle-to-cycle modulation underscores the importance of incorporating time-dependent transport and diffusivity variations in dynamo models to capture the full complexity of solar cycle amplitude modulation.

The present study assumes a simplified time profile for the BMR source with constant model parameters and a strictly periodic cycle of 11 years. While this facilitates clear comparison and the derivation of empirical trends, future work could benefit from incorporating cycle-to-cycle variations and in-cycle variation of SFT parameters to assess the impact of realistic variability on quenching efficiency and dipole moment buildup. Such a study could be extended to reconstruct the solar mag-

netic flux buildup as observed by various telescopes over the past several decades.

6. CONCLUSIONS

In this work, we examined the buildup of the solar dipole moment within a flux-transport dynamo framework using PINN simulations. By introducing the residual dipole moment, defined as $D_t - e^{-P/\tau} D_{\text{cycle min}}$, we isolated the net amplification within each cycle. The sensitivity analysis of ΔD_{LQ} and ΔD_{TQ} clarified how the relative contributions from LQ and TQ vary across the dynamo parameter space. We found that ΔD_{LQ} decreases systematically with diffusivity η but increases with meridional flow speed u_0 , while ΔD_{TQ} remains comparatively insensitive to η but grows modestly with u_0 . The ratio $\Delta D_{LQ}/\Delta D_{TQ}$ highlights the transport-dependent balance between these two mechanisms. The weak sensitivity of the dipole evolution to τ in PINN modulation indicates that nonlinear feedbacks dominate over the decay term in constraining the buildup of the polar dipole moment.

We present a possible scenario of complex interplay between the LQ and TQ in regulating the solar dipole moment from cycle to cycle. The quenching mechanisms influence the poleward transport of magnetic flux, with the efficiency of this migration depending on the cycle strength and the underlying dynamic parameters (meridional flow and diffusion). This nonlinear interplay could naturally produce an alternation between weak and strong cycles, giving rise to the observed even-odd cycle pattern.

An important aspect of this study is the application of PINN, which naturally embeds the governing equations into the learning process. Unlike conventional numerical schemes that rely on fine discretisation and face stability constraints, PINN achieve efficient and accurate representation of the solution across the full parameter space. This makes them especially well-suited for capturing nonlinear feedback in the solar dynamo while remaining computationally efficient and adaptable for data-driven extensions.

Our results provide a framework for linking dynamo simulations with observations. Sunspot emergence latitudes, tilt angle catalogues, and synoptic magnetograms can serve as complementary probes of LQ and TQ, while polar field measurements provide direct validation of their impact. Future cycle-dependent analyses of these datasets will allow the empirical testing and refinement of the quenching dependencies identified here, enabling data-constrained separation of LQ and TQ contributions to solar cycle variability.

In summary, nonlinear quenching mechanisms play a decisive role in regulating the solar dynamo and the buildup of the large-scale magnetic field. The interplay between LQ, TQ, and transport processes determines the effective range of dynamo operation and governs the strength of the polar field—the primary precursor of solar cycle predictability. By combining physical constraints with data-driven flexibility, PINN offers a powerful pathway towards more realistic and robust dynamo modelling, with direct implications for forecasting solar cycle variability and space weather impacts. This framework paves the way for data-constrained PINN solar cycle forecasts, incorporating WSO synoptic magnetograms and upcoming high-resolution observations from DKIST, thereby bridging theoretical modelling with observational constraints.

ACKNOWLEDGEMENTS

J.J.A. would like to express gratitude for the financial support received through the Prime Minister’s Research Fellowship. Part of this work was supported by *ESO*, project number Ts 17/2-1. Authors would also like to acknowledge the support of the ISRO RESPOND Grant (ISRO/RES/2/436/21-22).

Software: DeepXDE (Lu et al. 2021), Numpy (Harris et al. 2020), SciPy (Virtanen et al. 2020) and Matplotlib (Hunter 2007)

AUTHOR CONTRIBUTIONS

All authors contributed equally to this project.

APPENDIX

A. ERROR METRICS

Let y_i denote the observed (true) value, \hat{y}_i the predicted value by the model, \bar{y} the mean of the observed values and n the total number of data points.

$$\text{Mean Absolute Error (MAE)} = \frac{1}{n} \sum_{i=1}^n |y_i - \hat{y}_i| \quad (\text{A1})$$

$$\text{Mean Squared Error (MSE)} = \frac{1}{n} \sum_{i=1}^n (y_i - \hat{y}_i)^2 \quad (\text{A2})$$

$$\text{Root Mean Squared Error (RMSE)} = \sqrt{\frac{1}{n} \sum_{i=1}^n (y_i - \hat{y}_i)^2} \quad (\text{A3})$$

$$\text{Coefficient of Determination (}R^2\text{)} = 1 - \frac{\sum_{i=1}^n (y_i - \hat{y}_i)^2}{\sum_{i=1}^n (y_i - \bar{y})^2} \quad (\text{A4})$$

$$\text{Maximum Absolute Error (Max Error)} = \max_i |y_i - \hat{y}_i| \quad (\text{A5})$$

$$\text{Mean Absolute Percentage Error (MAPE)} = \frac{100\%}{n} \sum_{i=1}^n \left| \frac{y_i - \hat{y}_i}{y_i} \right| \quad (\text{A6})$$

The corresponding values of these error metrics are summarized in Table 2. The distribution of the error metrics for each model is shown in Figure 5.

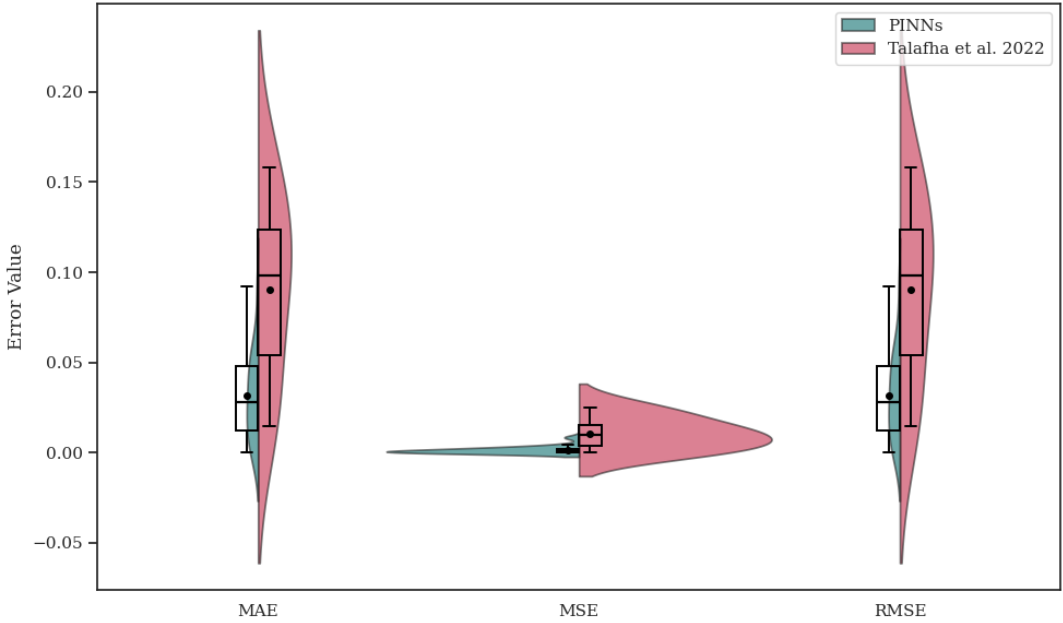


Figure 5. Distribution of errors for the PINNs model (teal) and Talafha et al. (crimson) across different metrics. Violin plots illustrate the full distributions of the errors, while overlaid boxplots highlight the median (horizontal line), mean (black circle), and interquartile range (box) for each metric.

B. ORDER-OF-MAGNITUDE SCALING OF THE SFT EQUATION

To obtain the scaling form of Equation (1), we perform a standard order-of-magnitude analysis using the characteristic quantities $B \sim B_*$, $t \sim t_*$, $u \sim u_0$, and $\partial/\partial\lambda \sim 1/\lambda$, where λ denotes heliographic latitude in radians and $\cos \lambda = \mathcal{O}(1)$ over the activity belts. The corresponding characteristic scales of the various terms are

$$\frac{\partial B}{\partial t} \sim \frac{B_*}{t_*}, \quad \frac{1}{R} \frac{\partial(Bu)}{\partial\lambda} \sim \frac{u_0 B_*}{R\lambda}, \quad \frac{\eta}{R^2} \frac{\partial^2 B}{\partial\lambda^2} \sim \frac{\eta B_*}{R^2 \lambda^2}, \quad \frac{B}{\tau} \sim \frac{B_*}{\tau}.$$

Balancing these terms and multiplying by R/u_0 yields the non-dimensional, order-of-magnitude form of the SFT equation,

$$\frac{R}{u_0} \frac{\partial B}{\partial t} \simeq \frac{B}{\lambda} + \left(\frac{\lambda_R}{\lambda} \right)^2 B - \frac{R}{u_0 \tau} B + \frac{R}{u_0} S, \quad (\text{B7})$$

Equation (B7) corresponds to the scaling relation used in Eq. (18) of the main text. Here, the terms respectively quantify advection (B/λ), diffusion [$(\lambda_R/\lambda)^2 B$], decay [$BR/(u_0\tau)$], and the source contribution [SR/u_0]. For typical solar parameters ($u_0 \sim 10\text{--}20 \text{ m s}^{-1}$, $\eta \sim 250\text{--}500 \text{ km}^2 \text{ s}^{-1}$), one finds $\lambda_R \sim 7^\circ \sim 15^\circ$, indicating that the large-scale field evolution is primarily governed by the balance between advection and diffusion within the activity belts.

REFERENCES

Abreu, J. A., Beer, J., Ferriz-Mas, A., McCracken, K. G., & Steinhilber, F. 2012, *Astronomy & Astrophysics*, 548, A88

Athalathil, J. J., Vaidya, B., Kundu, S., Upendran, V., & Cheung, M. C. 2024, *The Astrophysical Journal*, 975, 258

Babcock, H. 1961, *Astrophysical Journal*, vol. 133, p. 572, 133, 572

Bhowmik, P., Jiang, J., Upton, L., Lemerle, A., & Nandy, D. 2023, *Space Science Reviews*, 219, 40

Cameron, R. H., Schmitt, D., Jiang, J., & Işık, E. 2012, *A&A*, 542, A127

Charbonneau, P. 2010, *Living Reviews in Solar Physics*, 7, 3, doi: [10.12942/lrsp-2010-3](https://doi.org/10.12942/lrsp-2010-3)

Charbonneau, P. 2014, *Annual Review of Astronomy and Astrophysics*, 52, 251

Charbonneau, P., Beaubien, G., & St-Jean, C. 2007, *The Astrophysical Journal*, 658, 657

Charbonneau, P., & Sokoloff, D. 2023, *Space Science Reviews*, 219, 35

Charbonneau, P., St-Jean, C., & Zacharias, P. 2005, *ApJ*, 619, 613, doi: [10.1086/426385](https://doi.org/10.1086/426385)

Chen, Y., Dong, B., & Xu, J. 2022, *Journal of Computational Physics*, 455, 110996, doi: <https://doi.org/10.1016/j.jcp.2022.110996>

Choudhuri, A. R. 2021, *Science China Physics, Mechanics & Astronomy*, 64, 239601

—. 2023, *Reviews of Modern Plasma Physics*, 7, 18

Conti, P., Guo, M., Manzoni, A., et al. 2024, *Proceedings of the Royal Society A: Mathematical, Physical and Engineering Sciences*, 480, doi: [10.1098/rspa.2023.0655](https://doi.org/10.1098/rspa.2023.0655)

Dasi-Espuig, M., Solanki, S. K., Krivova, N. A., Cameron, R., & Peñuela, T. 2010, *A&A*, 518, A7, doi: [10.1051/0004-6361/201014301](https://doi.org/10.1051/0004-6361/201014301)

Deng, L., Li, B., Xiang, Y., & Dun, G. 2015, *The Astronomical Journal*, 151, 2

Falas, S., Konstantinou, C., & Michael, M. K. 2020, in 2020 IEEE 38th International Conference on Computer Design (ICCD), IEEE, 37–40

Fox, W., Sharma, B., Chen, J., Castellani, M., & Espino, D. M. 2024, *Fluids*, 9, 279

Gholampour, M., Hashemi, Z., Wu, M. C., et al. 2024, *International Communications in Heat and Mass Transfer*, 159, 108330

Guo, Y., Cao, X., Peng, K., et al. 2023, in *International Conference on Artificial Neural Networks*, Springer, 230–242

Harris, C. R., Millman, K. J., van der Walt, S. J., et al. 2020, *Nature*, 585, 357, doi: [10.1038/s41586-020-2649-2](https://doi.org/10.1038/s41586-020-2649-2)

Hathaway, D. H., Wilson, R. M., & Reichmann, E. J. 1994, *Sol. Phys.*, 151, 177

Hunter, J. D. 2007, *Computing in Science and Engineering*, 9, 90, doi: [10.1109/mcse.2007.55](https://doi.org/10.1109/mcse.2007.55)

Jha, B. K., Karak, B. B., & Banerjee, D. 2022, *Proceedings of the International Astronomical Union*, 18, 86

Jha, B. K., Karak, B. B., Mandal, S., & Banerjee, D. 2020, *ApJL*, 889, L19, doi: [10.3847/2041-8213/ab665c](https://doi.org/10.3847/2041-8213/ab665c)

Jiang, J. 2020, *ApJ*, 900, 19, doi: [10.3847/1538-4357/abaa4b](https://doi.org/10.3847/1538-4357/abaa4b)

Jiang, J. 2023, *Proceedings of the International Astronomical Union*, 19, 98

Jiang, J., Cameron, R. H., Schmitt, D., & Schüssler, M. 2011, *Astronomy & Astrophysics*, 528, A82

Jiang, J., Cameron, R. H., Schmitt, D., & Schüssler, M. 2011a, *A&A*, 528, A82, doi: [10.1051/0004-6361/201016167](https://doi.org/10.1051/0004-6361/201016167)

—. 2011b, *A&A*, 528, A82, doi: [10.1051/0004-6361/201016167](https://doi.org/10.1051/0004-6361/201016167)

Jiang, J., Cameron, R. H., & Schüssler, M. 2014, *ApJ*, 791, 5, doi: [10.1088/0004-637X/791/1/5](https://doi.org/10.1088/0004-637X/791/1/5)

Jiang, J., Hathaway, D., Cameron, R., et al. 2014, *Space Sci. Rev.*, 186, 491

Karak, B. B., & Miesch, M. 2018, *ApJL*, 860, L26, doi: [10.3847/2041-8213/aaaca97](https://doi.org/10.3847/2041-8213/aaaca97)

Karak, B. B., & Miesch, M. S. 2017, *The Astrophysical Journal*, 847, 69, doi: [10.3847/1538-4357/aa8636](https://doi.org/10.3847/1538-4357/aa8636)

Khalid, S., Yazdani, M. H., Azad, M. M., et al. 2024, *Mathematics*, 13, 17

Kingma, D. P., & Ba, J. 2014, CoRR, abs/1412.6980. <https://api.semanticscholar.org/CorpusID:6628106>

Kovachki, N., Li, Z., Liu, B., et al. 2021, arXiv e-prints, arXiv:2108.08481, doi: [10.48550/arXiv.2108.08481](https://doi.org/10.48550/arXiv.2108.08481)

Leighton, R. B. 1964, *Astrophysical Journal*, vol. 140, p. 1547, 140, 1547

—. 1969, *Astrophysical Journal*, vol. 156, p. 1, 156, 1

Lemerle, A., & Charbonneau, P. 2017, *ApJ*, 834, 133, doi: [10.3847/1538-4357/834/2/133](https://doi.org/10.3847/1538-4357/834/2/133)

Lenz, C., Bause, M., Henke, C., & Trächtler, A. 2024, in 2024 International Conference on Advanced Robotics and Mechatronics (ICARM), IEEE, 290–295

Li, K. J., Wang, J. X., Zhan, L. S., et al. 2003, *SoPh*, 215, 99, doi: [10.1023/A:1024814505979](https://doi.org/10.1023/A:1024814505979)

Li, T., Pan, Y., Chen, L., Xiong, B., & Li, M. 2024, in Proceedings of the 2024 3rd International Conference on Frontiers of Artificial Intelligence and Machine Learning, 352–355

Li, Z., Kovachki, N., Azizzadenesheli, K., et al. 2020, arXiv e-prints, arXiv:2010.08895, doi: [10.48550/arXiv.2010.08895](https://doi.org/10.48550/arXiv.2010.08895)

Li, Z., Zheng, H., Kovachki, N., et al. 2021, arXiv e-prints, arXiv:2111.03794, doi: [10.48550/arXiv.2111.03794](https://doi.org/10.48550/arXiv.2111.03794)

Liu, D. C., & Nocedal, J. 1989, *Mathematical Programming*, 45, 503, doi: [10.1007/bf01589116](https://doi.org/10.1007/bf01589116)

Lu, L., Meng, X., Mao, Z., & Karniadakis, G. E. 2021, *SIAM Review*, 63, 208, doi: [10.1137/19m1274067](https://doi.org/10.1137/19m1274067)

Madhavan, V., Sebastian, A. S., Ramsundar, B., & Viswanathan, V. 2024, doi: [10.48550/ARXIV.2407.06209](https://doi.org/10.48550/ARXIV.2407.06209)

Markidis, S. 2021, *Frontiers in big Data*, 4, 669097

Martin-Belda, D., & Cameron, R. H. 2017, *A&A*, 597, A21

Moschou, S., Hicks, E., Parekh, R., et al. 2023, *Machine Learning: Science and Technology*, 4, 035032

Nagovitsyn, Y. A., Osipova, A., & Ivanov, V. 2024, *Astronomy Reports*, 68, 89

Nagy, M., Lemerle, A., Labonville, F., Petrovay, K., & Charbonneau, P. 2017, *Sol. Phys.*, 292, 1

Parker, E. N. 1955, *Astrophysical Journal*, vol. 122, p. 293, 122, 293

—. 1958, *Astrophysical Journal*, vol. 128, p. 664, 128, 664

Petrovay, K. 2020, *Living Rev. Sol. Phys.*, 17, 2, doi: [10.1007/s41116-020-0022-z](https://doi.org/10.1007/s41116-020-0022-z)

Petrovay, K., Nagy, M., & Yeates, A. R. 2020, *JSWSC*, 10, 50, doi: [10.1051/swsc/2020050](https://doi.org/10.1051/swsc/2020050)

Petrovay, K., & Talafha, M. 2019, *A&A*, 632, A87, doi: [10.1051/0004-6361/201936099](https://doi.org/10.1051/0004-6361/201936099)

Schrijver, C. J., De Rosa, M. L., & Title, A. M. 2002, *ApJ*, 577, 1006, doi: [10.1086/342247](https://doi.org/10.1086/342247)

Sekii, T., & Shibahashi, H. 2015, *Extraterrestrial Seismology*, 180

Shuang, Z., Yong, F., Wen-Yuan, W., et al. 2015, *Acta Physica Sinica*, 64, 24

Solanki, S. K., Wenzler, T., & Schmitt, D. 2008, *A&A*, 483, 623, doi: [10.1051/0004-6361:20054282](https://doi.org/10.1051/0004-6361:20054282)

Song, Y., Wang, H., Yang, H., Taccari, M. L., & Chen, X. 2024, *Journal of Computational Physics*, 501, 112781

Steenbeck, M. 1966, *Z. Naturforsch.*, 21, 369

Talafha, M., Nagy, M., Lemerle, A., & Petrovay, K. 2022, *A&A*, 660, A92

Talafha, M. H. 2025, *Solar Physics*

Talafha, M. H., Petrovay, K., & Opitz, A. 2025, *Solar Physics*, 300, 1

Teweldebirhan, K., Miesch, M., & Gibson, S. 2024, *Solar Physics*, 299, 42

Tlatov, A. G., & Pevtsov, A. A. 2010, *Mem. Soc. Astron. Italiana*, 81, 814, doi: [10.48550/arXiv.1008.0185](https://doi.org/10.48550/arXiv.1008.0185)

Tobias, S. M. 2009, *The Origin and Dynamics of Solar Magnetism*, 77

Ulrich, R. K., & Boyden, J. E. 2005, *The Astrophysical Journal*, 620, L123, doi: [10.1086/428724](https://doi.org/10.1086/428724)

Vasil, G. M., Lecoanet, D., Augustson, K., et al. 2024, *Nature*, 629, 769

Virtanen, P., Gommers, R., Oliphant, T. E., et al. 2020, *Nature Methods*, 17, 261, doi: [10.1038/s41592-019-0686-2](https://doi.org/10.1038/s41592-019-0686-2)

Wang, B., Qin, A. K., Shafei, S., et al. 2023, in 2023 International Joint Conference on Neural Networks (IJCNN), IEEE, 1–7

Wang, Y.-M., Nash, A., & Sheeley Jr, N. 1989, *ApJ*, 347, 529

Yang, M., & Foster, J. T. 2022, *Computer Methods in Applied Mechanics and Engineering*, 402, 115041

Yeates, A. R., Bertello, L., Pevtsov, A. A., & Pevtsov, A. A. 2025, *The Astrophysical Journal*, 978, 147

Yeates, A. R., Cheung, M. C., Jiang, J., Petrovay, K., & Wang, Y.-M. 2023, *Space Sci. Rev.*, 219, 31

Zhang, J., Braga-Neto, U., & Gildin, E. 2024, *Energy & Fuels*, 38, 17781

Zhong, W., & Meidani, H. 2025, *Computer Methods in Applied Mechanics and Engineering*, 434, 117540, doi: [10.1016/j.cma.2024.117540](https://doi.org/10.1016/j.cma.2024.117540)

Zou, Z., Meng, X., & Karniadakis, G. E. 2024, *Journal of Computational Physics*, 505, 112918